OE Optical Engineering

RESEARCH PAPER

Fabrication and analysis of electrically large Luneburg lenses using vision-controlled material jetting

Colin Bonner,[a,*] **Zachary Nelson**,[b] **Desai Chen**,[b] **Liam Schwartz**,[b] **Scott Twiddy**,[b] **Batuhan Alasahin**,[a] **Michael Richards**,[a] **and Mark Mirotznik**[a]

[a]University of Delaware, Electrical and Computer Engineering, Newark, Delaware, United States
[b]Inkbit, Medford, Massachusetts, United States

ABSTRACT. We present the design, fabrication, and characterization of electrically large Luneburg lens (LL)-based antennas realized through vision-controlled inkjet-based additive manufacturing. Utilizing a low-loss cyclic olefin thermoset resin compatible with high-resolution material jetting, we demonstrate the fabrication of wideband gradient-index (GRIN) lenses operating at frequencies up to 100 GHz with apertures exceeding 30 wavelengths and realized gains exceeding 34 dBi. The spatially graded permittivity profiles were implemented using subwavelength diamond and gyroid lattice structures, with unit cell dimensions ranging from 2 to 5 mm. Effective medium theory, electromagnetic simulations, and calibration measurements were used to correlate lattice geometry with dielectric properties. Full-wave simulations and experimental gain measurements reveal the impact of unit cell size, material loss, and minimum achievable permittivity on realized performance. The fabricated LLs exhibit high aperture efficiencies and broad operational bandwidths, with experimental results closely matching theoretical and simulated predictions. This work demonstrates the viability of scalable inkjet 3D printing for next-generation, high-frequency GRIN-based antennas and highlights key design tradeoffs for achieving optimal performance in electrically large LL antennas.

Keywords: additive manufacturing; lens antennas; Luneburg lens; material jetting.

Paper 20251010G received Nov. 25, 2025; revised Jan. 16, 2026; accepted Jan. 20, 2026; published Feb. 25, 2026.

1 Introduction

The Luneburg lens (LL) is a spherically symmetric graded-index (GRIN) structure that transforms a spherical wavefront produced by a feed source on its surface into a highly directive, collimated beam.[1] This makes it an attractive platform for antenna applications requiring beam steering, wide angular coverage, and low sidelobe levels. Traditionally, LLs have been physically realized using concentric dielectric shells of discrete permittivity values to approximate the ideal GRIN distribution.[2,3] However, these conventional fabrication methods are costly to produce and poorly approximate the ideal distribution, resulting in reduced lens performance. Additive manufacturing (AM) presents a favorable alternative, presenting increased design freedom and the ability to construct continuous or discretized GRIN profiles composed of complex unit-cell geometries.[4–6] Despite this potential, most AM-enabled Luneburg lens antennas have remained electrically small and constrained in operational bandwidth[7–9] or are limited to discrete

*Address all correspondence to Colin Bonner, colibonn@udel.edu

permittivity values,[10] primarily due to limitations in printer resolution, available dielectric property range, and material loss.

In this work, we introduce a production-capable AM-based fabrication method[15] using novel low-loss printable dielectrics to realize electrically large LL-based antennas with aperture diameters greater than 30 times the operational free space wavelength (i.e., 32λ) operating at frequencies up to 100 GHz. Specifically, we utilized a commercial computer vision-controlled inkjet 3D printer that offers rapid, multimaterial fabrication with high spatial resolution and is capable of accurately producing hundreds of complex electromagnetic structures such as GRIN lenses per build. Commercial inkjet 3D printing employs printheads adapted from the 2D printing industry to precisely deposit picoliter-scale droplets, which then cure through thermal, chemical, or photochemical polymerization.[16–18]

Inkjet printing has previously been demonstrated for microwave devices, including LL antennas.[7] However, to date, no low-loss [$\tan(\delta) < 0.005$] printable dielectrics suitable for this platform have been reported. Most inkjet-compatible resins rely on reactive monomers (e.g., acrylates, epoxies, isocyanates, and thiol-enes) that yield high densities of polar groups within the cured material. Thus leading to dielectric losses exceeding $\tan(\delta) > 0.01$ at radio frequency (RF) and microwave frequencies. Although these losses can be mitigated in stereolithography systems by incorporating high-volume fractions of low-loss fillers (e.g., silica, PTFE),[13] such approaches are incompatible with inkjet systems due to strict viscosity constraints (<20 cP).[19] To overcome this limitation, we employed a novel nonpolar inkjet-printable resin based on cyclic olefin thermoset (COT) chemistry, recently developed by Inkbit. This resin utilizes nonpolar cyclic olefin monomers polymerized via ring-opening metathesis polymerization (ROMP), which yields low-loss dielectric properties favorable for RF applications.[20] Although the potential of cyclic olefin systems in AM has been recognized in prior literature, this work represents the first reported use of such a material to fabricate geometrically complex dielectric structures, including GRIN lenses.

We evaluate the performance of the resulting electrically large LL antennas through full-wave simulations and experimental validation. Key design parameters—including dielectric loss tangent, effective permittivity range, and unit-cell geometry—are investigated for their impact on lens performance. Although such parameters have limited influence on electrically small lenses, they become critical at larger apertures where wavefront aberrations and gain degradation are more pronounced. Our results reveal a saturation threshold in performance beyond which further increases in lens size yield diminishing returns due to material properties and geometric limitations.

The remainder of this paper is organized as follows. Section 2 provides theoretical background on Luneburg lenses. Section 2.1 derives the ideal gain profile, which serves as a reference benchmark. Section 2.2 introduces effective medium theory and its role in achieving a target GRIN distribution/. Section 2.4 addresses the frequency limitations imposed by unit-cell size and its geometry. Sections 2.3 and 2.5 examine the effects of material loss tangent and limited permittivity range, respectively, supported by full-wave simulations. A summary of the impacts of all previous subsections is provided in Sec. 2.6. Section 3 details the experimental methodology, including lens fabrication (Sec. 3.1), design approach (Sec. 3.2), and wideband measurement procedures (Sec. 3.3). Section 4 summarizes the key findings, discusses the results, and highlights the novel contributions of this work.

2 Theoretical Background

2.1 Theoretical Gain of an Ideal Luneburg Lens

The relative permittivity distribution of an ideal spherical LL is described by the classical Luneburg formulation,[1]

$$\varepsilon_{\mathrm{LL}}(r) = 2 - \left(\frac{r}{R}\right)^2, \tag{1}$$

where R is the radius of the lens, and r is the radial distance from the lens center. At the lens boundary ($r = R$), the relative permittivity approaches unity ($\varepsilon = 1$), resulting in a continuous

transition to free space and achieving perfect impedance matching with the surrounding air medium.

The theoretical maximum gain of an LL antenna is realized when the aperture efficiency equals unity. Thus, for an ideal LL fed by a point source, the effective aperture equals the physical cross-sectional area given by

$$A_{\text{eff}} = \pi R^2. \tag{2}$$

The antenna gain G is defined by the ratio of the effective aperture to that of an isotropic reference, A_{iso}, where the effective aperture of the isotropic reference is equal to $\frac{\lambda^2}{4\pi}$, where λ is the free-space wavelength. Combining this with [Eq. (1)], the boresight gain of an ideal Luneburg lens fed by a point source is given by

$$G_{\text{ideal}} = \frac{4\pi A_{\text{eff}}}{\lambda^2} = \frac{4\pi^2 R^2}{\lambda^2}. \tag{3}$$

Equation (3) is used throughout the remainder of this manuscript when comparing the gain of realistic LL antennas to the theoretical maximum value.

2.2 Effective Medium Theory and Graded Index Devices

The graded permittivity of the LL can be achieved by engineering a subwavelength lattice with spatially varying unit cell geometries. By tailoring the size, shape, and fill fraction of these periodic structures, the local effective permittivity can be controlled, enabling smooth dielectric gradients that approximate a continuous refractive index profile. The physical realization of the subwavelength unit cells commonly takes the physical form of gyroids,[13] connected cubes,[7,9] space-filling curves,[11,12] and the diamond lattice,[14] as illustrated in Fig. 1.

To design a spatially varying lattice effective medium theory (EMT) is typically employed. EMT provides quantitative models for predicting the effective homogeneous electromagnetic properties of inhomogeneous subwavelength composite materials. Given the properties of the individual constituents—often air and printed material when using additive manufacturing—and their corresponding volume fractions, effective properties can be analytically predicted such as complex permittivity. The complex relative permittivity ($\hat{\varepsilon}_r$) of a material at a given frequency is defined as

$$\hat{\varepsilon}_r = \varepsilon_r' - j \cdot \varepsilon_r'' = \varepsilon_r'(1 - j\,\tan(\delta)), \tag{4}$$

where ε_r', ε_r'' and $\tan(\delta)$ denotes the real and imaginary components of the complex permittivity and loss tangent respectively.

One of the most common EMT models is the Maxwell–Garnett theory. Using Maxwell–Garnett, the effective permittivity of a composite consisting of a host (air) and inclusions (printed material) can be related to the constituents' properties by the following expression:[21]

$$\hat{\varepsilon}_{\text{MG}} = 1 + \frac{3v_f \cdot (\hat{\varepsilon}_i - 1)}{\hat{\varepsilon}_i + 2 - v_f \cdot (\hat{\varepsilon}_i - 1)}, \tag{5}$$

where v_f is the volume fill fraction of the inclusion (printed material) in the unit cell and $\hat{\varepsilon}_i$ is the complex relative permittivity of the printed material (inclusion). Using such EMT models,

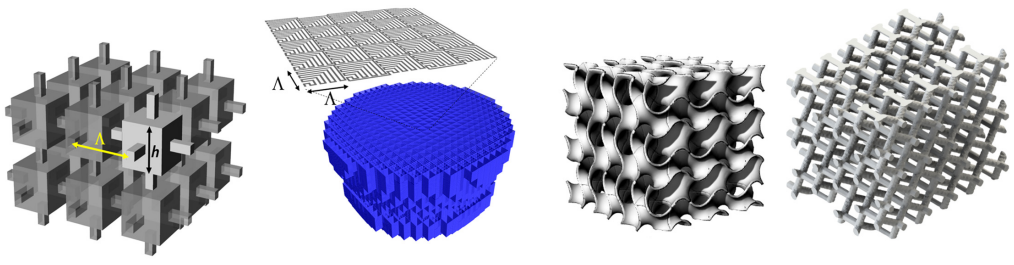

(a) (b) (c) (d)

Fig. 1 Common unit cell geometries (a) connected cubes,[7,9] (b) space filling curves,[11,12] (c) gyroids,[13] and (d) diamond lattice.[14]

composite lattices can be designed with effective dielectric properties ranging from near that of air (when v_f is small) up to that of the solid printed material (when v_f approaches 1.0), thereby producing the graded permittivity profile required for an LL.

While the theoretical LL antenna achieves 100% aperture efficiency with a realized gain given by [Eq. (3)] at any operational frequency, in practice the gain and operational bandwidth are constrained by several practical limitations. These include (a) size and shape of the unit cell, (b) minimum achievable permittivity, and (c) material losses. Each of these factors is described in the following sections.

2.3 Effect of Material Loss

Additive manufacturing (AM) enables the fabrication of complex and unconventional geometries that are often unattainable using traditional manufacturing techniques. However, the materials employed in certain AM processes can exhibit relatively high loss tangents,[22] which may significantly degrade electromagnetic performance. The impact of material loss on LL performance was investigated in detail in Ref. 23. In that study, material loss is accounted for using EMT to predict an effective loss tangent for the inhomogeneous air/material mixture comprising the lens. EMT was applied to the lossy LL permittivity distribution by setting $\varepsilon'_{\mathrm{MG}} \approx \varepsilon_{\mathrm{LL}}(r)$ where $\varepsilon_{\mathrm{LL}}(r)$ is the standard LL permittivity distribution given by [Eq. (1)] and solving for the spatially varying volume fraction $V_f(r)$

$$V_f(r) \approx \frac{2\varepsilon_{\mathrm{LL}}(r) - \varepsilon'_i + \varepsilon_{\mathrm{LL}}(r) - 2}{2\varepsilon'_i - \varepsilon_{\mathrm{LL}}(r) - 2}. \tag{6}$$

Substituting [Eq. (6)] into the Maxwell–Garnett equation [Eq. (5)] results in the effective permittivity distribution for the lossy LL.

This method was utilized to simulate the impact of material loss on the realized gain using the finite element method in COMSOL Multiphysics. For these simulations, an open-ended cylindrical waveguide, providing a circularly polarized excitation, was used to excite the lens. The lens model closely followed the permittivity distribution in [Eq. (1)] and was assumed to be isotropic. Due to symmetry about the z-axis, along which the waveguide is aligned, the full 3D simulation was reduced to a 2D axisymmetric model. This simplification significantly reduced computational time and resource requirements, allowing for the accurate analysis of electrically large LL antennas. The results shown in Fig. 2 demonstrate that with an increasing normalized lens radius, the loss of gain becomes increasingly significant, even for reasonably low-loss

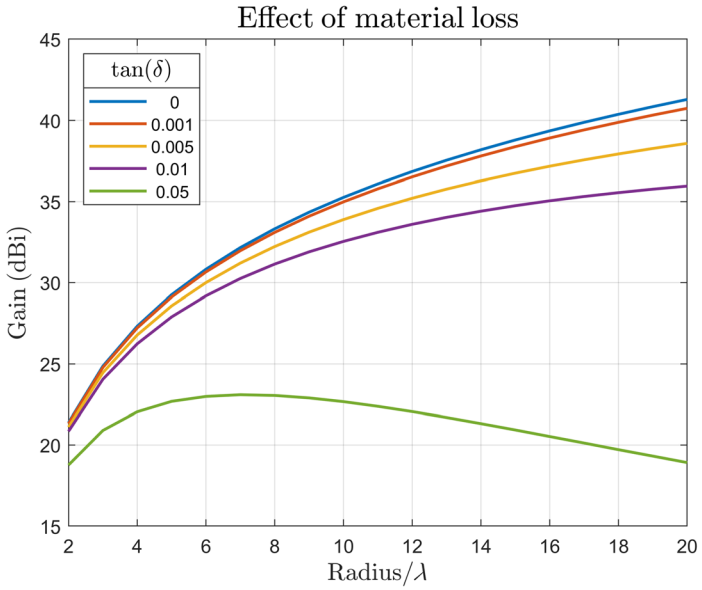

Fig. 2 Simulated realized gain of LL versus normalized lens radius as material loss tangent is varied.

Table 1 Dielectric constant and loss tangent of common materials used in 3D printing.

Material	ε'	$\tan(\delta)$
High density polyethylene[24] (30 GHz)	2.3	0.0002
Pure polycarbonate (PC)[22] (10 GHz)	2.59	0.0052
Acrylonitrile butadiene styrene (ABS)[22] (10 GHz)	2.54	0.006
DSM Somos NanoTool[22] (10 GHz)	3.2	0.0255
Rogers Radix[25] (24 GHz)	2.8	0.0046
***Inbkit* cyclic olefin resin V1 (60 GHz) [this study]**	**2.4**	**0.0032**
***Inbkit* cyclic olefin resin V2 (100 GHz)**	**2.4**	**0.0018**

materials. For reference, Table 1 provides the dielectric constant and loss tangent for several commonly used materials to print LL. For this work, Inkbit's cyclic olefin resin version 1 ($\tan(\delta) \approx 0.0032$ at 60 GHz) was used to fabricate all lenses.

2.4 Frequency Limitations Due to Unit-Cell Size and Geometry

The operational maximum frequency of graded-index (GRIN) devices is fundamentally constrained by the physical dimensions and geometry of their constituent unit cells.[21] As frequency increases (wavelength decreases), a point is reached where the unit cell is no longer electrically small, causing a breakdown of the effective medium approximation. To determine the frequency limits beyond which EMT fails, full-wave simulations were carried out using the frequency-domain solver in CST Studio Suite.[26] These simulations used the bulk material parameters employed in our fabrication approach and implemented periodic boundary conditions along the x- and y-directions, with Floquet ports on the z-plane boundaries. Only the fundamental mode was excited to ensure accurate characterization of the unit cell response. The model included a stack of five unit cells along the z-axis (to capture a representative volume), with infinite periodicity assumed in the transverse directions (see Fig. 3). Simulations were conducted for two fixed unit cell sizes of $l = 2$ and 5 mm. To tune the effective permittivity within the range $1 \leq \varepsilon'_{\mathrm{MG}} \leq 2$, structural parameters were varied parametrically— specifically, wall thickness for gyroid lattices, cube size for connected cube lattices, and beam radius for diamond lattices. In all simulations,

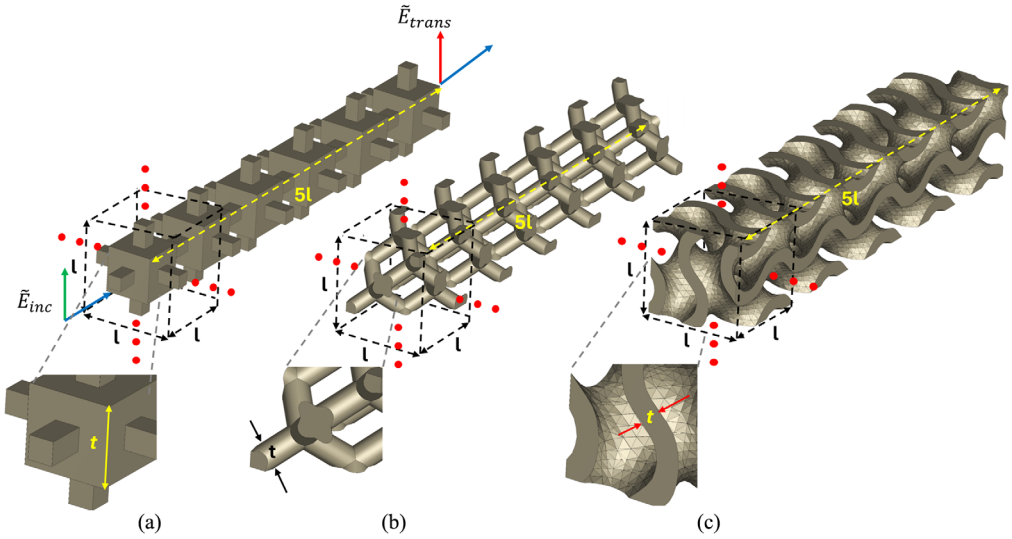

Fig. 3 Description of lattice models used to evaluate the validity of EMT (a) connected cube lattice, (b) diamond lattice and (3) gyroid lattice.

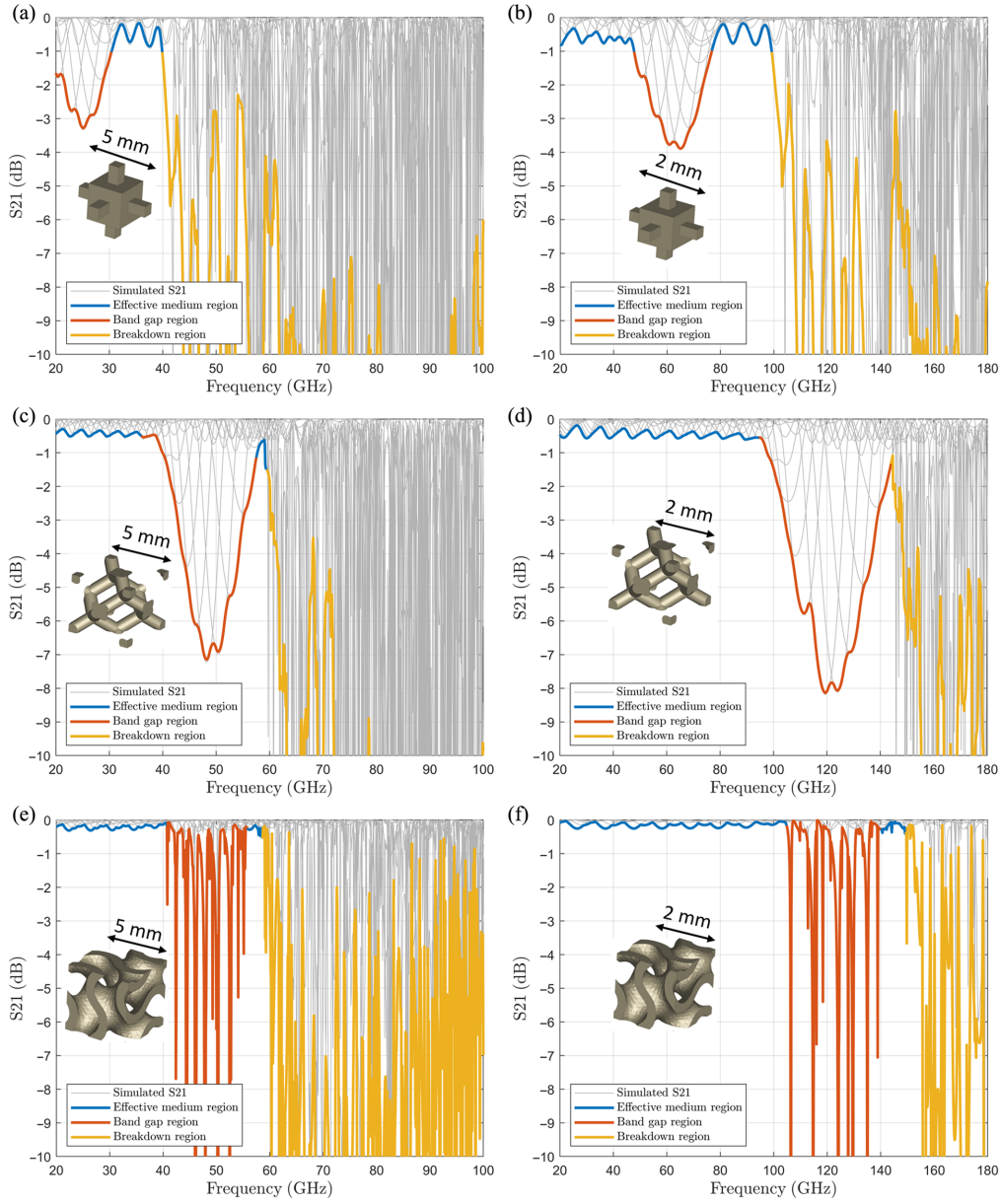

Fig. 4 Simulated transmission through 5 unit cells of connected cube lattice of 2 mm (a) and 5 mm (b) periods, diamond lattice of 2 mm (c) and 5 mm (d) periods, and gyroid lattice of 2 mm (e) and 5 mm (f) periods.

the real part of the permittivity of the cyclic olefin resin, given in Table 1, was assumed for the printed material.

Figure 4 presents the simulated transmission coefficient magnitudes (S_{21}) as a function of frequency for each of the three lattice structures investigated. The light gray traces correspond to individual simulations spanning a range of effective permittivities, whereas the solid-colored curves represent an envelope approximation corresponding to a GRIN structure composed of a continuous distribution of these effective properties. Three distinct frequency regions are observed across all geometries and are delineated by the color-coded envelopes: (1) an effective medium region, where EMT accurately describes the electromagnetic behavior; (2) a bandgap region, characterized by partial attenuation due to the onset of a weak photonic bandgap; and (3) a breakdown region, where scattering effects dominate and homogenization is no longer applicable. As expected, the transition frequencies between these regimes shift to higher values as the unit cell size decreases. Notably, for the diamond and gyroid lattices, the cubic unit cell

exhibits smaller primitive periodicities than those of the connected cubic. This results in the bandgap and breakdown regions for the diamond and gyroid lattices occurring at higher frequencies relative to the other two. Experimental results validating these predictions are presented in Sec. 3.

An interesting observation is that, in some cases, an effective medium region reemerges at frequencies above the bandgap but below the breakdown threshold. This intermediate high-frequency effective medium behavior could potentially extend the operational frequency range of the lens. It is important to note, however, that the present analysis is limited to wave propagation along one of the primary lattice axes. The relatively small dielectric contrast of the printed lattices used in Luneburg lenses (LLs) results in weak photonic bandgaps,[27] characterized by partial attenuation along specific crystallographic directions and, consequently, anisotropic wave propagation through the structure. However, unit cell geometries do exist that exhibit complete photonic bandgaps with small dielectric contrast.[28] Ongoing investigations are focused on characterizing this directional dependence in greater detail, and the results will be presented in a future manuscript.

2.5 Effect of Minimum Achievable Permittivity

The continuously graded index profile of the ideal LL is given by [Eq. (1)] smoothly approaches a relative permittivity of free space, which poses significant challenges for conventional gradient-index (GRIN) manufacturing techniques.[29–31] For instance, additive manufacturing techniques would require a fill fraction approaching zero near the lens boundary to achieve a relative permittivity approaching unity. However, such low fill fractions result in structures that lack mechanical integrity and cannot support themselves using conventional additive methods. Consequently, there exists a minimum realizable fill fraction for mechanical robustness and potentially a maximum value as well, due to material and process constraints. Taking these limitations into account, the physically realizable LL permittivity distribution is modified and takes the form:

$$\varepsilon_{\mathrm{LL}}(r) = \varepsilon_{\max} + (\varepsilon_{\min} - \varepsilon_{\max})\left(\frac{r}{R}\right)^2, \tag{7}$$

where $\varepsilon_{\max}$ and $\varepsilon_{\min}$ denote the maximum and minimum achievable relative permittivity, respectively. This modified formulation accounts for the practical limitations of additive manufacturing while still approximating the ideal Luneburg lens profile. In the literature, LLs have been fabricated and characterized that exhibit a minimum relative permittivity of $\varepsilon_{\min} = 1.15$,[29] $\varepsilon_{\min} = 1.2$,[30] and $\varepsilon_{\min} = 1.4$.[31] In this work, our printed lattice designs achieved values of $\varepsilon_{\min} = 1.11$ and $\varepsilon_{\min} = 1.04$ for the 2 and 5 mm unit cells, respectively.

To determine the impact of this permittivity mismatch on antenna performance, we conducted rigorous electromagnetic simulations using the finite element method with the COMSOL Multiphysics[32] model described previously. This analysis was performed for a range of lossless lenses radii R that were normalized to the free space wavelength λ. The minimum permittivity $\varepsilon_{\min}$ was swept parametrically from 1.0 to 1.16, whereas the maximum permittivity was fixed at $\varepsilon_{\max} = 2.0$ for all cases. The resulting realized antenna gains are shown in Fig. 5.

As the normalized lens radius increases, the effect of the exterior boundary impedance mismatch becomes increasingly detrimental to gain performance. For small to moderately sized lenses $(R/\lambda < 5)$, this effect remains minimal, even under severe mismatch conditions. However, for electrically large LL-based antennas $(R/\lambda > 5)$, gain degradation becomes increasingly more substantial, even with relatively modest impedance mismatches. Notably, when the minimum relative permittivity is elevated $(\varepsilon_{\min} > 1.1)$, a point of diminishing returns arises, wherein increasing the lens diameter leads to a decrease in realized gain rather than an improvement. Reference 33 presents an analytical solution that optimizes the maximum relative permittivity $(\varepsilon_{\max})$ to compensate for elevated $\varepsilon_{\min}$, thereby restoring gain performance for larger apertures. Nonetheless, practical limitations imposed by available materials and additive manufacturing processes often constrain the maximum achievable permittivity, making it challenging to fully mitigate mismatch effects in electrically large lenses.

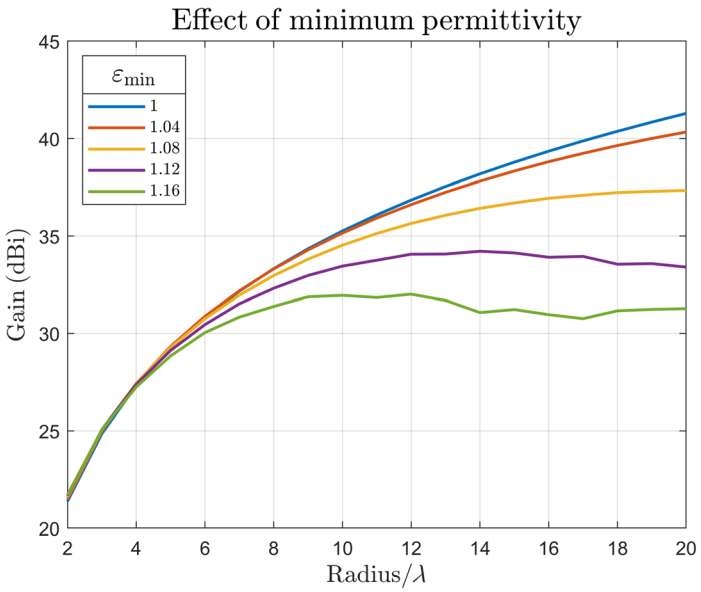

Fig. 5 Simulated realized gain of LL versus normalized lens radius as minimum permittivity at lens–air interface is varied with a constant maximum permittivity of 2.

2.6 Summary of Modeling Results

The modeling results presented in this section can be used to establish performance bounds of electrically large, additively manufactured Luneburg lenses. Starting from the ideal permittivity profile and gain of a perfect Luneburg lens, effective medium theory, particularly the Maxwell–Garnett model, was used to relate subwavelength lattice geometries to spatially graded dielectric properties. This enabled practical GRIN lens design using 3D-printable unit cells. Material loss was incorporated into this model, showing that even reasonably low-loss dielectrics can limit gain in large-aperture designs due to cumulative absorption effects.

Full-wave simulations further quantified the impact of unit cell size and geometry, revealing three distinct operational regimes: homogenization, weak bandgap, and breakdown. These transitions depend on lattice type and frequency and impose upper limits on lens performance. Additional analysis showed that a minimum achievable permittivity at the lens–air interface introduces impedance mismatch, reducing gain at large electrical sizes. Together, these models highlight critical design tradeoffs and establish practical limits for achieving high-gain, broadband operation in 3D-printed Luneburg lenses. The following sections present the fabrication of electrically large LL lens antennas and experimental measurements that validate the modeling predictions.

3 Experimental Methods

To validate the theoretical predictions, we fabricated several Luneburg lenses using the vision-controlled material-jetting process and characterized their performance across multiple frequency bands. The experimental methodology is detailed in the following subsections.

3.1 Lens Fabrication Using Vision-Controlled Material Jetting

Electrically large LLs were fabricated using Inkbit Vista, an inkjet-based additive manufacturing platform developed by Inkbit. The fabrication process comprises three primary steps, as outlined below. Although a detailed description of the Inkbit Vista material jetting process is provided in Ref. 15, a summary is included here and illustrated in Fig. 6(a).

The fabrication process comprises three primary steps:

3.1.1 *Layer-by-layer multimaterial deposition*

During printing, picoliter droplets of three distinct fluids are deposited onto a moving build platform as it passes beneath three arrays of inkjet printheads. Two of these fluids are build materials

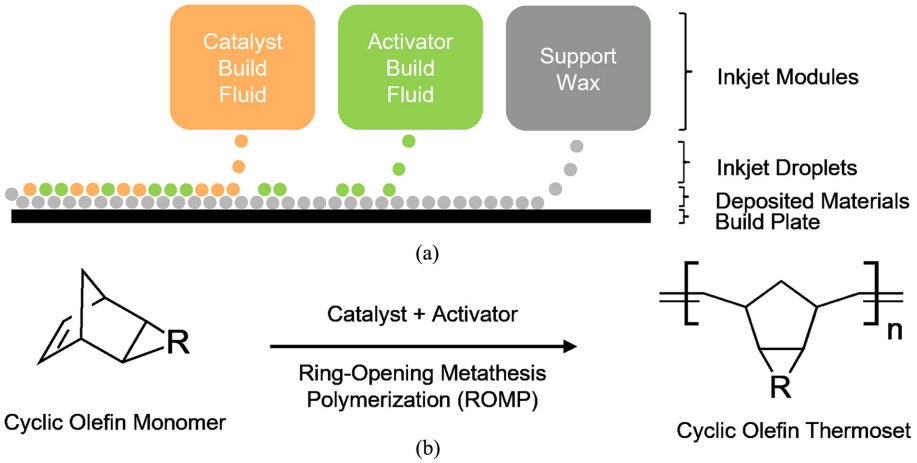

Fig. 6 (a) Representation of the fabrication process in which droplets are ejected from inkjet modules, deposited onto a build plate, and then chemically hardened (resins) or frozen (wax) to form each layer. The process repeats thousands of times to form a Luneburg lens. (b) Reaction scheme by which liquid cyclic olefin monomers are transformed into solid cyclic olefin thermosets via ring-opening metathesis polymerization (ROMP). The group R represents many possible variations of aliphatic hydrocarbon functional groups.

(which harden upon curing to form the final part), and the third is a phase-change support material (a wax that solidifies upon cooling to support overhangs). The printer's software governs the deposition pattern for each layer. As the build plate shuttles back and forth, droplets of the two liquid resins and wax are selectively deposited according to the slice data. Each deposited layer is then exposed to the appropriate curing condition (chemical/ thermal for the resins and cooling for the wax) before the next layer is applied. This sequence repeats thousands of times to form the complete Luneburg lens [Fig. 6(a)].

3.1.2 *In situ* polymerization *of the resin*

The two build fluids consist primarily of a proprietary formulation containing norbornene-functionalized cyclic olefin monomers (>98% by mass in the cured solid), a non-reactive solvent (<2%), a Grubbs-type ruthenium precatalyst (<100 ppm), a chemical activator (<50 ppm), and other minor additives (<0.1%). One of the build fluids contains the Ru pre-catalyst, whereas the other contains the activator. When the two fluids co-deposit and mix on the build plate, they undergo *in situ* chemical activation, initiating a ring-opening metathesis polymerization (ROMP) that cures the resin into a cross-linked cyclic olefin thermoset network [Fig. 6(b)]. This on-demand polymerization approach (enabled by the separated catalyst/activator system) ensures that curing occurs rapidly and locally after deposition, yielding a solid part with the desired low-loss dielectric properties.

3.1.3 *Postprocessing and cleanup*

After printing is complete, the entire part (embedded in solidified wax support) is removed from the printer. The part is first immersed in a bath of molten support material (65°C) for 30 min to liquefy the bulk of the wax support. Next, the part is transferred to a thermal fluid bath at 115°C for a period to complete any remaining polymerization and fully cure the polymer. Finally, residual surface contaminants are removed using a commercial halogenated-solvent vapor degreasing system. For lenses composed of the finer 2 mm unit cell lattice, an additional cleaning step is implemented prior to the final thermal cure: the parts are submerged in heated thermal fluid at 80°C and subjected to ultrasonic agitation (37 kHz for 15 min) to help remove wax from the small lattice voids. (This additional step was found to improve the cleanliness of the 2 mm lattice lenses before final curing.)

Using this process, objects can be printed with a total build volume of ($449 \times 236 \times 212$ mm) with a minimum feature size of 100 to 300 μm. This technique enables parallel

fabrication, allowing for the production of up to 112 lenses with a 62 mm diameter or 16 lenses with 100 mm diameter within a 24-h period.

3.2 Lens Design

The fabricated LLs employed spatially varying lattices based on diamond and gyroid unit cells according to the dielectric properties of the Inkbit cyclic olefin resin (see Table 1). The unit cells for the diamond lattices were generated from the diamond cubic crystal structure with a unit cell length of l [Fig. 3(b)]. Around each vertex, a sphere mesh of radius t and around each line connecting vertices, a cylinder mesh of radius t were generated. For the lens based on the gyroid lattice, the unit cells were generated by solving the trigonometric approximation of the gyroid surface given in [Eq. (8)] for one unit cell volume. The resulting surface was thickened to thickness t [Fig. 3(c)]. Lattices were generated by tiling space with the unit cells within volumes defined by a provided mesh (e.g., from an STL file). Using this process, lattices could be fully defined with parameters for the unit cell length (l), beam radius or thickness (t),

$$\sin(x)\cos(y) + \sin(y)\cos(z) + \sin(z)\cos(x) = 0. \tag{8}$$

To correlate the lattice parameters with the effective dielectric constant, calibration samples ($150 \times 150 \times 3$ mm) were printed where $l = 2$ mm, the lattice type was diamond, and beam radius, t, varied between 175 and 600 μm. The effective complex dielectric constants of latticed sheets and a solid control were measured using a microwave-focused beam system (MFBS) produced by Compass Technology Group.[34] The measured dielectric constant was found to be relatively flat across the frequency bands of interest (e.g., 26 to 110 GHz) while the loss tangent for the bulk sample was below 0.005 across this range. These results are summarized in Table 2. Reasonably good agreement was found between the experimental and predicted effective dielectric constant calculated using the Maxwell–Garnett expression given by [Eq. (5)].

After calibration, the spherical LLs were designed using the expression given in [Eq. (7)] where the maximum permittivity value was set to 2.0, and the minimum permittivity value was set to 1.11 and 1.04 for the 2 and 5 mm unit cells, respectively.

Five Luneburg lenses were fabricated for experimental testing, as summarized in Table 3. These included two diameters (62 and 100 mm) and two lattice unit cell sizes (2 and 5 mm) using the diamond lattice, as well as a 62 mm lens using a 5 mm gyroid lattice. Figure 7 shows images of two of the lenses with associated high-resolution scans via micro-CT, highlighting the internal lattice structure.

3.3 Experimental Characterization

Linearly polarized realized gain measurements were performed at three frequency bands—Ka, U, and W—by mounting the lenses onto a rotary stage, allowing rotation in the azimuth (H) plane

Table 2 Calibration results and comparison to EMT predictions.

Beam radius (μm)	Measured v_f	Measured ε_{eff}	Calculated ε_{eff}	Error (%)
175	0.129	1.16	1.13	2.7
200	0.248	1.29	1.26	2.6
250	0.317	1.38	1.33	3.2
350	0.382	1.46	1.41	3.2
400	0.494	1.61	1.56	3.2
500	0.624	1.79	1.74	2.6
600	0.854	2.14	2.12	1.0
Solid	1.0	2.40	2.40	n/a

Table 3 Fabricated lenses.

Fabricated LL	Diameter (mm)	Unit cell size (mm)	Lattice type
1	62.0	2.0	Diamond
2	62.0	5.0	Diamond
3	100.0	2.0	Diamond
4	100.0	5.0	Diamond
5	62.0	5.0	Gyroid

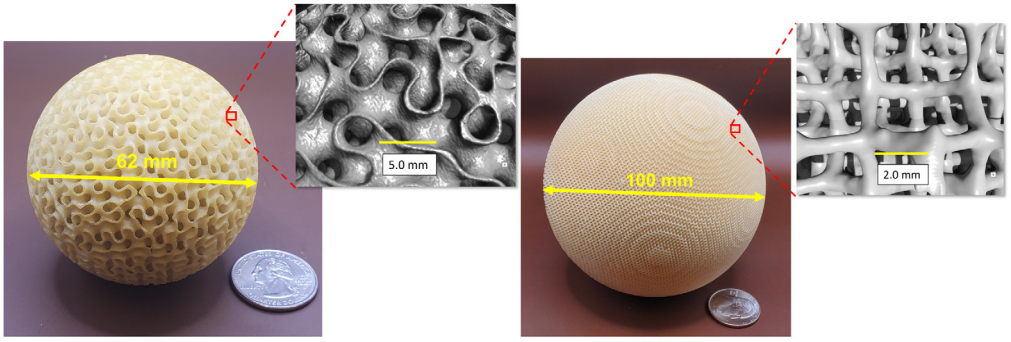

Fig. 7 Photograph of (a) 62 mm diameter lens (gyroid lattice, 5 mm unit cell) and (b) 100 mm diameter luneburg lens (diamond lattice, 2 mm unit cell). Micro-CT cross-sectional scans for each lens illustrate the internal lattice structure.

relative to the feed antenna from −60 deg to 60 deg. The Ka–band measurements were performed relative to a rectangular horn antenna (QuinStar QWH_APRS00) using a Rohde & Schwarz ZNB 40 vector network analyzer (VNA) with an open-ended rectangular waveguide-to-coaxial adapter (WR28) used as a feed for the lens. U-band measurements were made relative to a rectangular horn antenna (Eravant SAR201319S2WP), using an Agilent Technologies E8361C VNA, with an open-ended WR-19 rectangular waveguide-to-coaxial adapter employed as the antenna feed. W-band measurements were conducted using an Agilent Technologies E8364B VNA integrated with OML millimeter-wave extenders. These measurements were performed relative to a rectangular horn antenna (Pasternack PEWAN1017), which also served as the antenna feed. Variations in gain across the frequency bands of the rectangular horn antennas used for calibration were accounted for by simulating each antenna in CST Studio Suite using the frequency domain solver. The resulting simulated boresight gain profiles were used to correct the measured data to obtain more accurate realized gain values.

The corrected measured realized gain data for the five LLs is presented in Fig. 8. The 2 mm unit cell length LLs [Figs. 8(a) and 8(b)] exhibit an initial dip in boresight gain around 100 GHz, closely aligning with the trend predicted by the unit cell analysis in Fig. 4(b), demonstrating ultra-wideband high gain performance. Likewise, the 5 mm unit cell size lenses [Figs. 8(c)–8(e)] show strong agreement with the expected behavior. Namely, an initial gain drop near 37 GHz, followed by a local minimum around 45 GHz, which corresponds to the intrinsic bandgap of the unit cell. A subsequent recovery in boresight gain is observed at approximately 50 GHz, with a final breakdown region occurring near 60 GHz – consistent with the simulation results that predict breakdown of effective medium properties in the 5 mm unit cell simulations.

In Fig. 9, we present line scans of the realized gain patterns from Fig. 8 at three representative frequencies (30, 60, and 90 GHz) along with tabulated boresight data in Table 4. The results highlight the similar boresight gain and sidelobe characteristics among the different lens configurations at lower frequencies, indicating that all designs maintain comparable performance in terms of peak gain and relative sidelobe level.

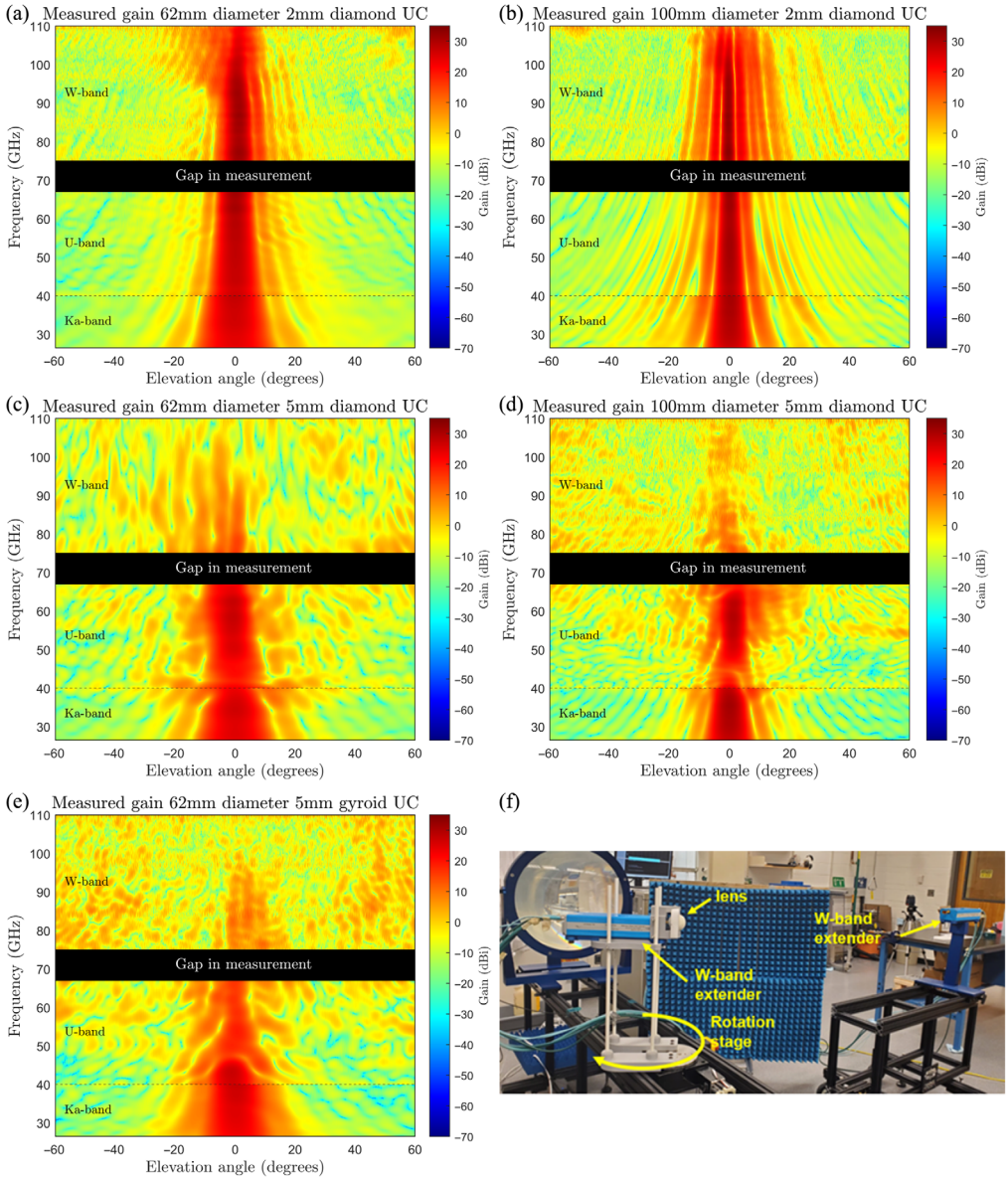

Fig. 8 Wide band measured linearly polarized realized gain of luneburg lenses across the elevation plane for (a) lens of 62 mm diameter with a diamond lattice of unit cell size of 2 mm, (b) 100 mm diameter with a diamond lattice with a unit cell size of 2 mm, (c) 62 mm diameter with a diamond lattice with a unit cell size of 5 mm (d) 100 mm diameter with a diamond lattice with a unit cell size of 5 mm, (e) 62 mm diameter with a gyroid lattice of unit cell size of 5 mm and (f) test setup for measuring radiation patterns.

S_{11} measurements were also performed, with the reference plane calibrated to the coaxial interface of the open-ended waveguide-to-coaxial adapter. Across all lens and feed combinations, the return loss remained below −13 dB throughout the expected operational frequency range of each unit cell, consistent with the predictions shown in Fig. 4.

The simulation techniques described in Secs. 2.3 and 2.5 were employed to evaluate the performance of the fabricated lenses, incorporating both manufacturing constraints and material property limitations. Although these simulations account for performance degradation due to dielectric loss and impedance mismatch, they do not explicitly model the unit cell geometry. As a result, phenomena such as bandgap and EMT breakdown, both governed by the unit cell architecture, are absent from the simulated data.

Figure 10(a) presents the results of these simulations alongside experimentally measured boresight gain data for all four lenses. To enable direct comparison, the measured gain was

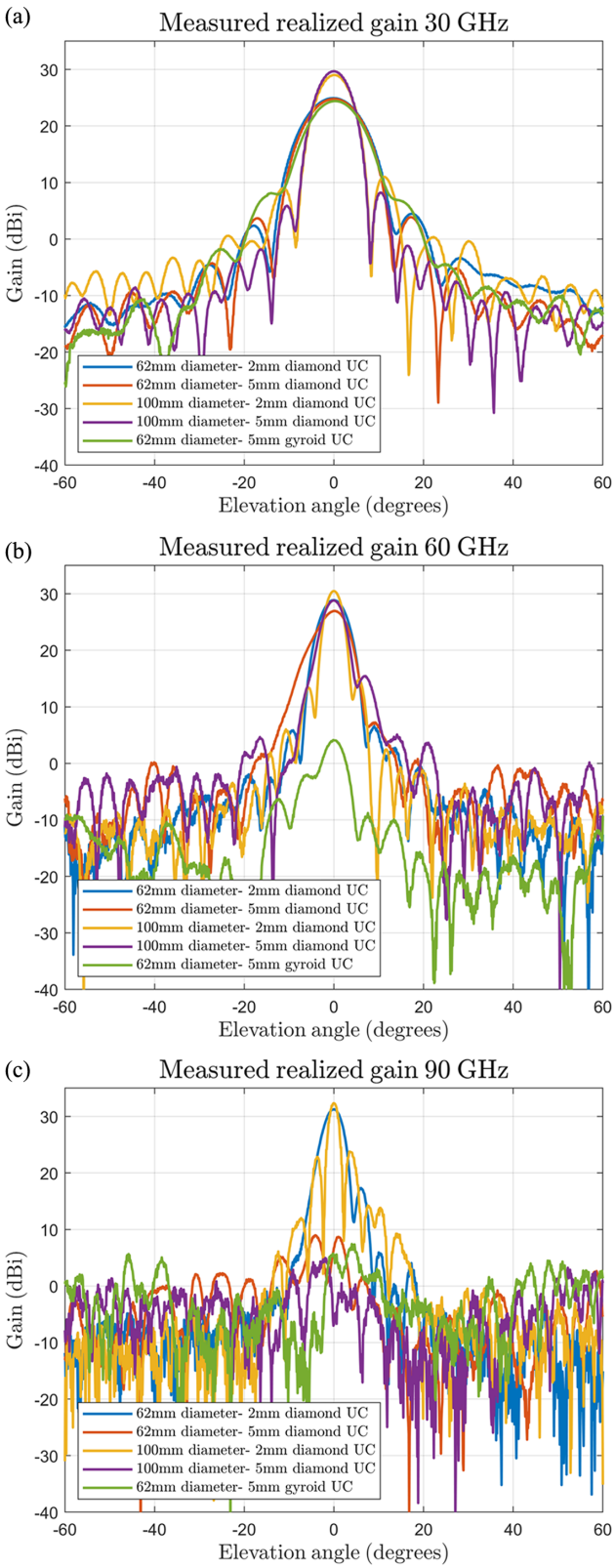

Fig. 9 Realized gain for five fabricated luneburg lenses described in Table 3 at (a) 30 GHz, (b) 60 GHz, and (c) 90 GHz.

Table 4 Maximum realized gain (G_0) and relative side lobe levels (RSLL).

	30 GHz	60 GHz	90 GHz
	G_0/RSLL	G_0/RSLL	G_0/RSLL
LL #1	24.9 dBi	28.8 dBi	31.2 dBi
2 mm diamond	−20.5 dB	−22.4 dB	−14 dB
LL #2	24.8 dBi	27 dBi	NA
5 mm diamond	−21 dB	−19.8 dB	
LL #3	29 dBi	30.5 dBi	32.4 dBi
2 mm diamond	−18.9 dB	−15.7 dB	−8.7 dB
LL #4	29.7 dBi	28.8 dBi	NA
5 mm diamond	−21.7 dB	−13.6 dB	
LL #5	24.4 dBi	4 dBi	NA
5 mm gyroid	−17.6 dB	−6 dB	

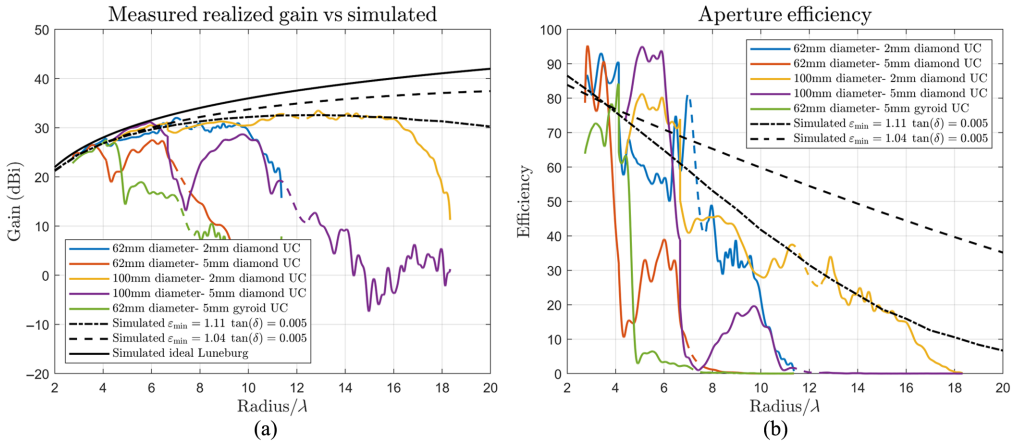

Fig. 10 Simulated and measured realized gain (a) and aperture efficiency (b) versus noramalized radius, where the dashed colored lines represent data interopolated within the gap in our measurement system (i.e., 68 to 75 GHz).

normalized with respect to the lens radius. Across all cases, the measured data exhibited strong agreement with simulation results up to the onset of the unit cell bandgap, beyond which a marked decline in gain was observed. For reference, the theoretical gain of an ideal Luneburg lens as a function of normalized radius is also included in Fig. 10(a), illustrating the influence of fabrication and material constraints on realized performance.

Simulated results for the 2 mm unit cell configuration with a minimum permittivity of $\varepsilon'_{\text{min}} = 1.11$ indicate a maximum gain at a normalized radius of 12λ, which corresponds to the physical extent of the 100 mm lens. The experimental results for this lens exhibit strong agreement, with peak gain observed near 12λ (~72 GHz). Aperture efficiency, computed as the ratio of measured or simulated gain to that of an ideal Luneburg lens, was also evaluated as a function of normalized radius and is shown in Fig. 10(b). The measured efficiency trends closely follow those of the simulations, although local variations of ~10% to 15% are observed, likely due to alignment inaccuracies during testing.

4 Discussion/Conclusion

The electrically large wideband lenses demonstrated high gain at radii of 16λ and frequencies approaching 100 GHz. This was enabled by the combination of an inkjet 3D printing coupled with a low-loss dielectric resin. The maximum radius (R) of the Luneburg lens at the time of fabrication was due primarily to the maximum build volume dimensions of the printer. The build dimensions of inkjet printers can scale much larger; however, due to the limitations of the 2 mm diamond lattice unit cell, namely, the range of achievable permittivity and loss tangent of materials, the 100 mm lens already surpasses the point of diminishing returns, which occurs at roughly the maximum radius of 12λ or frequency of 72 GHz. However, larger unit cells such as the 5 mm could still greatly benefit from an increased build volume. Realizing high densities in such compact and complex geometries is also limited by support material removal after printing. Inkjet resins are by necessity about one to two orders of magnitude less viscous than other resin-based 3D printing technologies, specifically <20 cP for inkjet resins and 100 to 10,000 cP for typical stereo-lithography resins,[27] making inkjet fabrication methods more suitable for high-frequency lens fabrication.

Maximum gain was shown to be fundamentally limited by the loss tangent of the solid material. The loss tangent of Inkbit cyclic olefin thermoset was measured to be $\tan(\delta) \approx 0.005$ across the W-Band. This value is lower than the typical 3D-printed thermosets (> 0.01)[35] and comparable to other commercially available low-loss thermosets such as Rogers Radix (0.0046 at 24 GHz).[25] Therefore, the gain values reported herein are also attributable to the low loss tangent of the dielectric material. The cyclic olefin thermoset material achieves low dielectric loss because of the absence of heteroatoms in the cyclic olefin monomer structure, and so is intrinsically low loss. Future improvements to the cyclic olefin thermoset formulation may reduce the loss tangent further and enable the fabrication of Luneburg lenses with even greater values for maximum gain.

Disclosures

The authors declare that there are no financial interests, commercial affiliations, or other potential conflicts of interest that could have influenced the objectivity of this research or the writing of this paper.

Code and Data Availability

The data that support the findings of this study are not openly available due to privacy concerns and are available from the corresponding author upon reasonable request.

Acknowledgments

OpenAI's Chat GPT model was used for light grammatical editing and readability improvements.

References

1. R. K. Luneburg, *Mathematical Theory of Optics*, Brown University Press, Providence (1944).
2. B. Fuchs et al., "Design optimization of multishell luneburg lenses," *IEEE Trans. Antennas Propag.* **55**(2), 283–289 (2007).
3. S. Rondineau, M. Himdi, and J. Sorieux, "A sliced spherical luneburg lens," *IEEE Antennas Wireless Propag. Lett.* **2**, 163–166 (2003).
4. Z. Larimore et al., "Use of space-filling curves for additive manufacturing of three-dimensionally varying graded dielectric structures using fused deposition modeling," *Additive Manuf.* **15**, 48–56 (2017).
5. M. Norooziarab et al., "Millimeter-wave 3d printed luneburg lens antenna," in *IEEE Radio and Antenna Days Indian Ocean (RADIO)*, Reunion, France, pp. 1–2 (2019).
6. Y. Guo et al., "A. 3d printed nearly isotropic luneburg lens antenna for millimeter-wave vehicular networks," *IEEE Trans. Veh. Technol.* **71**(2), 1145–1155 (2022).
7. M. Liang et al., "A. 3-d luneburg lens antenna fabricated by polymer jetting rapid prototyping," *IEEE Trans. Antennas Propag.* **62**(4), 1799–1807 (2014).
8. A. Bahr et al., "3d-Printed Omnidirectional Luneburg Lens Retroreflectors for Low-Cost Mm-Wave Positioning," in *Proc. IEEE Int. Conf. RFID (RFID)*, Orlando, Florida, pp. 1–7 (2020).
9. S. Lei et al., "A design of broadband 3-d-printed circularly polarized spherical luneburg lens antenna for x-band," *IEEE Antennas Wireless Propag. Lett.* **20**(4), 528–532 (2021).

10. H. Giddens, A. S. Andy, and Y. Hao, "Multimaterial 3d-printed compressed luneburg lens for mm-wave beam steering," *IEEE Antennas Wireless Propag. Lett.* **20**(11), 2166–2170 (2021).
11. Z. Larimore et al., "Additive manufacturing of luneburg lens antennas using space filling curves and fused filament fabrication," *IEEE Trans. Antennas Propag.* **66**(6), 2818–2827 (2018).
12. T. Fessaras et al., "Wide-angle passive beam steering using 3d modified partial maxwell fisheye lens," *Opt. Express.* **32**(5), 6997–7011 (2024).
13. W. Wang, P. Lambert, and J. Chisum, "High-Frequency Limits for 3d-Printed Gradient-Index (grin) Lens Antennas," in *Proc. IEEE Int. Symp. Antennas Propag. USNC-URSI Radio Sci. Meeting*, pp. 1695–1696 (2023).
14. L. Hao et al., "Design and additive manufacturing of cellular lattice structures," in *Innovative Developments in Virtual and Physical Prototyping*, Leiria, Portugal (2011).
15. T. J. K. Buchner et al., "Vision-controlled jetting for composite systems and robots," *Nature* **623**(7987), 522–530 (2023).
16. V. Chovancova, A. Pekarovicova, and P. D. Fleming, "Hot melt inks for 3d printing," in *IS&T Digital Fabrication Conf.*, pp. 143–147 (2005).
17. P. Kröber et al., "Reactive inkjet printing of polyurethanes," *J. Mater. Chem.* **19**(29), 5234–5238 (2009).
18. J. Mueller, K. Shea, and C. Daraio, "Mechanical properties of parts fabricated with inkjet 3d printing through efficient experimental design," *Mater. Des.* **86**, 902–912 (2015).
19. E. P. Furlani, "Fluid mechanics for inkjet printing," in *Fundamentals of Inkjet Printing*, S. D. Hoath, Ed., pp. 13–56, Wiley (2016).
20. Y. Piro et al., "Low-loss dielectric ink for printed radio frequency and microwave devices," *ACS Appl. Mater. Interfaces.* **15**(29), 35449–35458 (2023).
21. A. Sihvola, *Electromagnetic Mixing Formulas and Applications*, The Institution of Engineering and Technology, London, UK (2008).
22. P. I. Deffenbaugh, R. C. Rumpf, and K. H. Church, "Broadband microwave frequency characterization of 3-D printed materials," *IEEE Trans. Components Packag. Manuf. Technol.* **3**(12), 2147–2155 (2013).
23. B. F. LaRocca and M. S. Mirotznik, "An empirical loss model for an additively manufactured luneburg lens antenna," *ACES J.* **37**, 554–567 (2022).
24. J. Krupka, "Measurements of the complex permittivity of low-loss polymers at frequency range from 5 ghz to 50 ghz," *IEEE Microw. Wireless Compon. Lett.* **26**(6), 464–466 (2016).
25. R. Corporation, *Advanced Electronics Solutions, Radix™ Printable Dielectric—3D-Printable Dielectric Material for Use on Fortify FLUX Series Printers* (2023).
26. Dassault Systèmes, Vélizy-Villacoublay, France, CST Studio Suite, *Electromagnetic Field Simulation Software*, ver. 2022 (2022).
27. J. D. Joannopoulos et al., *Photonic Crystals: Molding the Flow of Light*, 2nd ed., Princeton Univ. Press, Princeton, NJ (2008).
28. L. Maiwald et al., "Control over light emission in low-refractive-index artificial materials inspired by reciprocal design," *Adv. Opt. Mater.* **10**(1), 2100785 (2022).
29 M. K. Saleem et al., "Lens antenna for wide angle beam scanning at 79 ghz for automotive short-range radar applications," *IEEE Trans. Antennas Propag.* **65**(4), 2041–2046 (2017).
30. S. Manafi, J. M. F. González, and D. S. Filipovic, "Design of a perforated flat luneburg lens antenna array for wideband millimeter-wave applications," in *Proc. 13th Eur. Conf. Antennas Propag (EuCAP)*, Krakow, Poland, pp. 1–5 (2019).
31. L. Xue and V. F. Fusco, "Printed holey plate luneburg lens," *Microw. Opt. Technol. Lett.* **50**(2), 378–380 (2008).
32. COMSOL AB, "COMSOL Multiphysics® v. 5.6," Stockholm, Sweden, www.comsol.com.
33. V. Kaschten et al., "Mismatched luneburg lenses: numerical analysis and design rules," *IEEE Trans. Antennas Propag.* **72**(5), 4487–4500 (2024).
34. J. W. Schultz, *Focused Beam Methods*, John Schultz (2012).
35. D. Foster et al., "Printed materials and their effects on quasi-optical millimeter wave guide lens systems," in *Proc. Int. Solid Freeform Fabrication Symp.*, pp. 2104–2119 (2019).

Colin Bonner received his BS degree in electrical engineering in 2022 from the University of Delaware, where he is currently pursuing his PhD in electrical engineering. He was an undergraduate research assistant from 2020 to 2022. Since 2022, he has been a graduate research assistant with the Department of Electrical and Computer Engineering at the University of Delaware. His research interests include metamaterial lens and antenna design and fabrication, additive manufacturing, and electromagnetic material characterization.

Zachary Nelson received his BA degree in chemistry from Cornell University, Ithaca, New York, in 2015, and his PhD in chemistry from the Massachusetts Institute of Technology,

Cambridge, Massachusetts, in 2021. Since 2021, he has been a materials scientist at Inkbit, Medford, Massachusetts. His research interests include high-performance polymeric materials, molecular photophysics and optics, and method development for catalytic chemical transformations.

Desai Chen received his BS degree in computer science from Carnegie Mellon University, Pittsburgh, Pennsylvania, in 2011 and his PhD in computer science from the EECS Department at Massachusetts Institute of Technology, Cambridge, Massachusetts, in 2017. Since 2017, he has been working as a software research engineer at Inkbit, Medford, Massachusetts. His research focuses on computer graphics, 3D printing, computational geometry, machine vision, and finite element analysis.

Scott Twiddy received a MChem degree in chemistry in 2008 and a PhD in chemistry in 2012 both from The University of Southampton, UK. Since 2012, he has worked in several areas including pharmaceutical drug development, banknote anti-counterfeiting, and nearly a decade in materials development for additive manufacturing. Since 2019, he has served as Materials R&D Lead at Inkbit, Medford, MA focusing on new chemistries and processes for high performance 3D-printed polymers

Michael Richards received his BS degree in electrical engineering in 2021 and his MS degree in electrical and computer engineering in 2022, both from the University of Delaware. He is currently pursuing his PhD in electrical engineering at the University of Delaware. From 2019 to 2021, he was an undergraduate research assistant with the Department of Electrical and Computer Engineering at the University of Delaware. Since 2021, he has been a graduate research assistant in the same department. His research interests include transmission line modeling and design, antenna design, frequency-selective surfaces, additive manufacturing, and millimeter-wave imaging and sensing technologies.

Mark Mirotznik received his BSEE degree from Bradley University in 1988 and his MSEE and PhD degrees from the University of Pennsylvania in 1991 and 1992, respectively. From 1992 to 2009, he was a faculty member with the Department of Electrical Engineering, The Catholic University of America. Since 2009, he has been a professor and an associate chair at the University of Delaware and a senior research engineer at the Naval Surface Warfare Center.

Biographies of the other authors are not available.